NANOSTRUCTURED 3D BIOPRINTING OF PLA WITH BIOGLASS-CNT SCAFFOLDS FOR OSSEUS TISSUE GRAFT MANUFACTURING

JMR&T
2023

BIOMATERIAL

Writers
ESLEANE VILELA VASCONCELOS
FRANCILENE BELO DA LUZ
SIMONE PATRI´CIA ARANHA DA PAZ
MARCOS ALLAN LEITE DOS REIS
ALISSON CLAY RIOS DA SILVA
MARCELE FONSECA PASSOS
S ERGIO NEVES MONTEIRO

Available online at www.sciencedirect.com

jmr&t
Journal of Materials Research and Technology

journal homepage: www.elsevier.com/locate/jmrt

Original Article

Nanostructured 3D bioprinting of PLA with bioglass-CNT scaffolds for osseus tissue graft manufacturing

Esleane Vilela Vasconcelos [a], *Francilene Belo da Luz* [a], *Simone Patrícia Aranha da Paz* [a], *Marcos Allan Leite dos Reis* [a], *Alisson Clay Rios da Silva* [b], *Marcele Fonseca Passos* [b], *Carlos Augusto Galvão Barboza* [c], *Sérgio Neves Monteiro* [d], *Verônica Scarpini Candido* [a,*]

[a] *Engineering of Natural Resources of the Amazon Program, Federal University of Para, Belem, PA, 67030-007, Brazil*
[b] *Materials Science and Engineering Program, Federal University of Pará, Ananindeua, PA, 67130-660, Brazil*
[c] *Dental Science Program, Federal University of Rio Grande Do Norte, Av Salgado Filho, Natal, RN, 59072-970, Brazil*
[d] *Department of Materials Science, Military Institute of Engineering, Rio de Janeiro, RJ, 22290-270, Brazil*

ARTICLE INFO

Article history:
Received 4 November 2022
Accepted 22 February 2023
Available online 28 February 2023

Keywords:
PLA
Bioglass
Carbon nanotubes and 3D printing

ABSTRACT

Bone involvement promoted by aging and accidents has raised interest in biomaterials and biofabrication technologies for bone regeneration purposes. Thus, 3D printing technology has gained prominence in the production of scaffolds due to its versatility in producing complex geometries with interconnected pores. In this work, composite scaffolds of poly (lactic acid) (PLA), bioglass (BG) and carbon nanotubes (CNT) were produced by 3D printing, using hexagonal, honeycomb-like geometry interspersed. The samples were analyzed in terms of chemical structure, crystallinity and morphology using Fourier transform infrared spectroscopy and Raman spectroscopy, X-ray diffraction and scanning electron microscopy, respectively. The thermal stability of the composite was evaluated by thermogravimetry and the mechanical properties by compression tests. The cell viability was determined by Alamar Blue. The results that raman spectroscopy confirmed the interaction of BG in the polymer matrix by new peaks in the spectrum between 1400 and 2600 cm^{-1} and the presence of the D, G and 2D bands of the CNTs. In terms of compressive strength, PLA scaffolds with 2 mm inner spacing demonstrated higher compressive strength of 14.88 ± 2.35 MPa, while PLA/CNT higher apparent compressive modulus of 0.58 ± 0.36 GPa. In cell viability, statistical tests showed that there was no significant difference between scaffolds with 2 and 4 mm inner spacing.

* Corresponding author. Engineering of Natural Resources of the Amazon Program, Federal University of Para, Belem, PA, 67030-007, Brazil
E-mail address: scarpini.ve@gmail.com (V.S. Candido).

https://doi.org/10.1016/j.jmrt.2023.02.171

1. Introduction

Population aging causes an increase in degenerative diseases and fractures by accidents, which impact on people's quality of life. Thus, there is a great interest in the search for materials for bone reconstruction [1,2]. Among the main materials investigated, the biomaterials compatible with bone structure, such as poly (lactic acid) (PLA) and bioglass (BG) [3], stand out.

Among the methods of biomaterials production, there is the additive manufacturing. This technique has gained significant prominence due to the ability to produce combinations of materials with appropriate design for bone regeneration, such as porous scaffolds. The scaffolds are structures that act as a support for cell growth with the aim of regeneration of a new tissue and can be optimized by materials with properties of biodegradability, biocompatibility and bioactivity for bone improvement and replacement [4,5].

With regard to the 3D printing technique, we can quote the fused deposition modeling (FDM) to produce scaffolds, with the advantage of low cost, reproducibility, control of size, geometry, interconnectivity of the pores produced and the combination of materials that can be used in the process [6]. It is emphasized that the geometry and size of the pores are important factors that favor cell growth and differentiation and tissue vascularization [6,7].

With reference to the biomaterials available for bone regeneration, it is desirable that these present characteristics such as biocompatibility and bioreabsorption. Serra et al. [8] produced scaffolds de chitosan, gelatin and βTCP for bone regeneration and concluded that the scaffolds showed bioactivity and biocompatibility being potential materials for application in bone regeneration. Lee et al. [9] produced a chitosan biomaterial modified with nanoclay for application as a bone substitute and concluded that the material produced had osteoinductive effects, enhanced by the nanoclay, and provided the making of a favorable environment for bone healing. Popescu et al. [10] developed alginate-pullulan-glass-ceramic composite scaffolds for bone regeneration and concluded that the composite induced bone regeneration and angiogenesis in in vivo tests, increasing its osteogenic capacity. Gregor et al. [11] reported the biocompatibility of the scaffold produced by fused deposition modeling technique with commercially available poly (lactic acid) (PLA), presenting cytotoxicity tests, evaluation of cell proliferation and differentiation capacity with satisfactory results. The PLA is considered a promising biomaterial due to its biocompatibility, bioreabsorptivity and good mechanical strength, besides being easily processed and absorbed by the human body, qualities that make them attractive for the production of bone scaffolds [12,13].

Another material, widely used for bone regeneration is the bioglass (BG), a type of bioceramics that presents high properties of biocompatibility and osseointegration. Bioglass develops strong bonds with bone through the formation of a bone apatite layer on the surface, which releases Si, Ca, P, and Na ions, as well as stimulates bone tissue formation [14–16]. In this regard, de Souza et al. [17] have attested to the biocompatibility, bioactivity and bone regeneration in in vitro and in vivo experiments with bioglass.

One of the methods to obtain bioglass is the sol-gel, which is highly attractive for favoring the porosity of great interest for bone regeneration, besides being a simple and least cost method [16,18]. With regard to bioglass, it is known that it has limitations that come from its low mechanical strength, especially fracture toughness [19]. As a way of trying to remedy this situation, studies [20,21], point to the addition of carbon nanotubes (CNT) as reinforcement material, due to its excellent mechanical resistance [22]. In this case, Touri et al. [23] attested to the improved mechanical properties of the bioglass/CTN composite compared to the bioglass scaffold for bone tissue engineering.

Thus, the aim of this study was to produce and study PLA, PLA/BG and PLA/CNT scaffolds by FDM printing with honeycomb geometry, geometric shape that is indicated as favorable to cell growth and differentiation [24]. It is noteworthy that it is the first time that a biocomposite with this form of production and composition was produced, since it was not found in the literature of PLA, BG and CNT scaffold in interleaved honeycomb, produced by FDM printing, using bio-glass synthesized by organic sol-gel route.

2. Materials and methods

2.1. Bioactive glass synthesis

The bioglass was synthesized by the sol-gel method according to the methodology of Faure et al. [25] adapted. The following precursor chemicals were used: tetraethyl orthosilicate (TEOS) 11.6 ml, and triethyl phosphate (TEP) 1 ml, both from Sigma-Aldrich (SP/Brazil), calcium nitrate tetrahydrate 7.15 g, sodium nitrate 4.65 g and 5 mM citric acid solution, 26 ml from Dynamics (SP/Brazil). The reagents were mixed slowly in a thermostat reactor of the brand Thega (MG/Brazil) until the formation of a transparent gel. Afterwards, it was kept at 60 °C in a stove from the brand Gigante, model G42L (SP/Brazil), for 18 h and sintered at 200 °C for 5 h and 700 °C for 2 h in a Solidsteel muffle furnace, model SSfm (SP/Brazil). The obtained powder was sieved in a 100 Tyler sieve for particle size reduction, according to the diagram in Fig. 1.

2.2. Filament preparation

Transparent PLA filament with a diameter of 1.75 mm from 3D Fila® (MG/Brazil) was used. PLA (0.2 g) was solubilized in pure acetone mixed in a Schuster L100 ultrasonic washer (RS/Brazil) for 360 s with (0.007 g) carboxylic acid functionalized multi-walled carbon nanotubes. Then the same preparation was performed with the PLA solution and BG (0.016 g). The prepared solutions were used for coating the pure PLA filament by reverse immersion methodology (Fig. 2). To coat the PLA filament with the solutions, a funnel with a small hole and a thickness close to the diameter of the filament was used. One centimeter of the filament was inserted at the end of the funnel and the solution was added at the top of the funnel. Then, the filament was pulled upwards at 0.05 m/s until the entire useable length is coated with the CNT or BG solution. Afterwards, the filament was left for drying and adhesion at room temperature (RT) for 2 h. After this time, the inverted

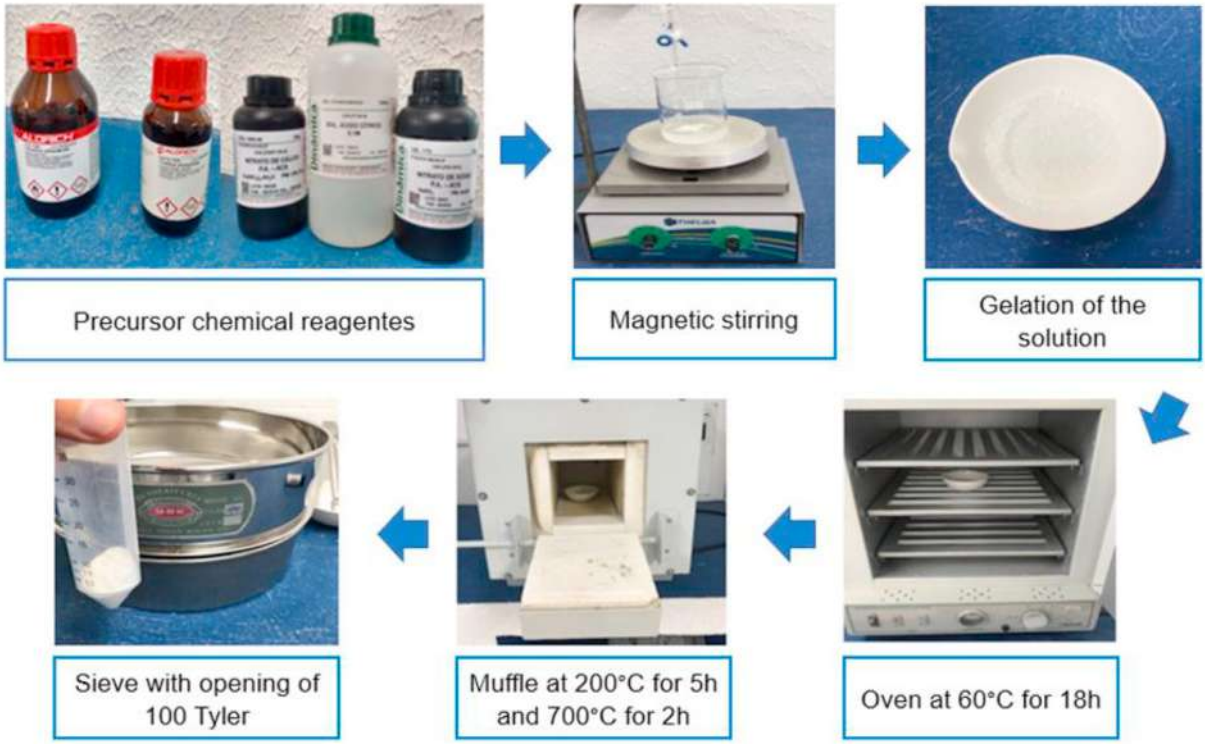

Fig. 1 – Schematic diagram of bioglass synthesis by the sol-gel method.

dipping procedure was performed again, thus coating the filament again with a second layer superimposed on the previous one. After this process, the filament was separate for drying in at RT for another 5 h. After that period, ready to use in the printer.

During printing, the filament with the surface coated with CNT or BG undergoes a melting process at 210 °C in the printer's extruder nozzle, thus ensuring that the nanoparticles deposited on the surface of the filament are also part of the entire polymeric matrix.

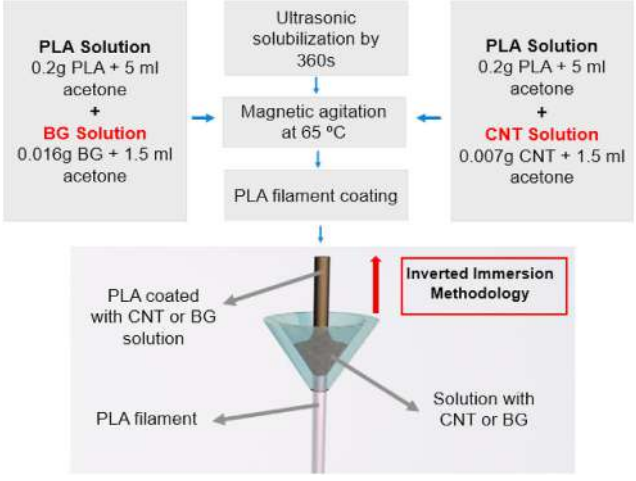

Fig. 2 – Scheme of preparation of solutions for coating filaments for 3D printing.

2.3. *3D printing of scaffolds by fused deposition modeling (FDM)*

A commercial FDM printer of the brand Stella3 LITE (PR/Brazil) was used to fabricate the scaffolds. The selected interleaved honeycomb architecture forming hexagons was designed by the Cinema 4D modeling software (free version) and the printing parameters were set by the Prusa-Slicer slicer version 2.3.2 (free version). Fig. 3 shows the design of the scaffolds. The 3D scaffolds were prepared via bedding layer deposition by melt extrusion of PLA filament with a 0.2 mm diameter extruder nozzle. The temperature of the initial layer was 210 °C and the temperature of the other layers was 180 °C,

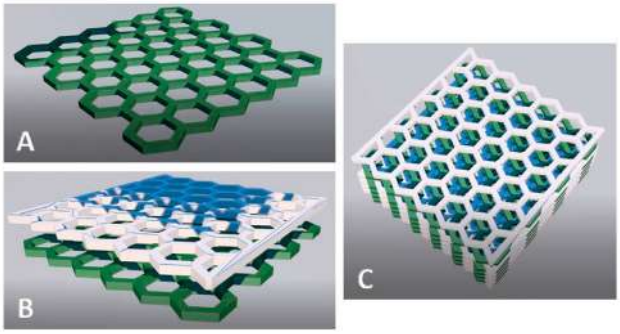

Fig. 3 – Layer-by-layer scaffold design with hexagonal honeycomb geometry. In A, the first layer is observed on a certain axis. In B, the posterior layer in the displaced axis so that the hexagons are in the center of the previous layer, in this way, the intercalation of the layers shown in C.

with a layer thickness of 0.1 mm and a wall thickness of 0.4 mm. The printing speed for the outer part was 20 mm/s and for the inner part was 10 mm/s, and scaffolds with inner spacing, between filaments, of 2 and 4 mm of PLA, PLA/BG, and PLA/CNT were produced (Fig. 4).

2.4. *Thermal impregnation of the scaffold surface*

To induce increased cell adhesion, the PLA, PLA/BG and PLA/CNT scaffolds were coated with bioglass in order to cover the entire surface. To do so, the samples were placed in petri dishes and covered with the powder, and then placed in a stove at a temperature of 130 °C with an average heating rate of 4.8 °C/min, followed by convection cooling.

2.5. *Description*

2.5.1. *X-ray diffraction (XRD)*

Qualitative crystalline phases were obtained by XRD, in Proto Manufacturing equipment, XRD Powder Diffraction System: the generator of 30 kV and 2 mA, Cu-Kα1 radiation, angular step of 0.0149°, time interval of 0.5 s, sweep of 47 min and 2θ ranging from 5° to 60°. The crystalline phases in the residue were identified with reference to COD. The test was performed on the bioglass samples and the PLA, PLA/BG and PLA/CNT filaments.

2.5.2. *Fourier transform infrared vibrational spectroscopy (FTIR)*

A Thermo Scientific Nicolet iS50 FTIR spectrophotometer was used for FTIR. The samples were analyzed in the mid-infrared spectral region (MIR - Middle Infrared), from 4000 to 400 cm-1. The test was performed on the bioglass sample.

2.5.3. *Scanning electron microscopy (SEM)*

The bioglass and scaffolds were metallized with Au/Pd using a QUORUM TECHNOLOGIES SC7620 metallizer and then observed under a TESCAN VEGA 3 scanning electron microscope with an electron beam current of 85–90 μA, acceleration voltage of 15 kV and WD of 15 mm. The test was performed on the bioglass samples and the PLA, PLA/BG and PLA/CNT scaffolds before and after impregnation with BG on the surface. The pore size in the filaments was measured by SEM, according to Fig. 5.

2.5.4. *Raman spectroscopy*

For the Raman scattering measurements, it was used the LabRam Spectrometer equipment HR Evolution model from Horiba, under the following conditions: Laser of 633 nm; Range of 600–3200 cm-1; Time of 120 s; Accumulations of 2; Laser Power Filter of 5% and, Lens of 100x. The tests were performed on the bioglass samples and PLA, PLA/BG and PLA/CNT scaffolds before and after thermal impregnation with BG on the surface.

2.5.5. *Thermogravimetric analysis*

The thermogravimetric analysis (TGA) and its derivative (DTG) was performed in Shimadzu equipment of the model DTG-60H. The test was performed under a continuous oxygen atmosphere at 50 ml/min, at a heating rate of 20 °C/min, from RT up to 800 °C. The test was performed on the PLA/CNT scaffold sample impregnated with BG on the surface to evaluate the

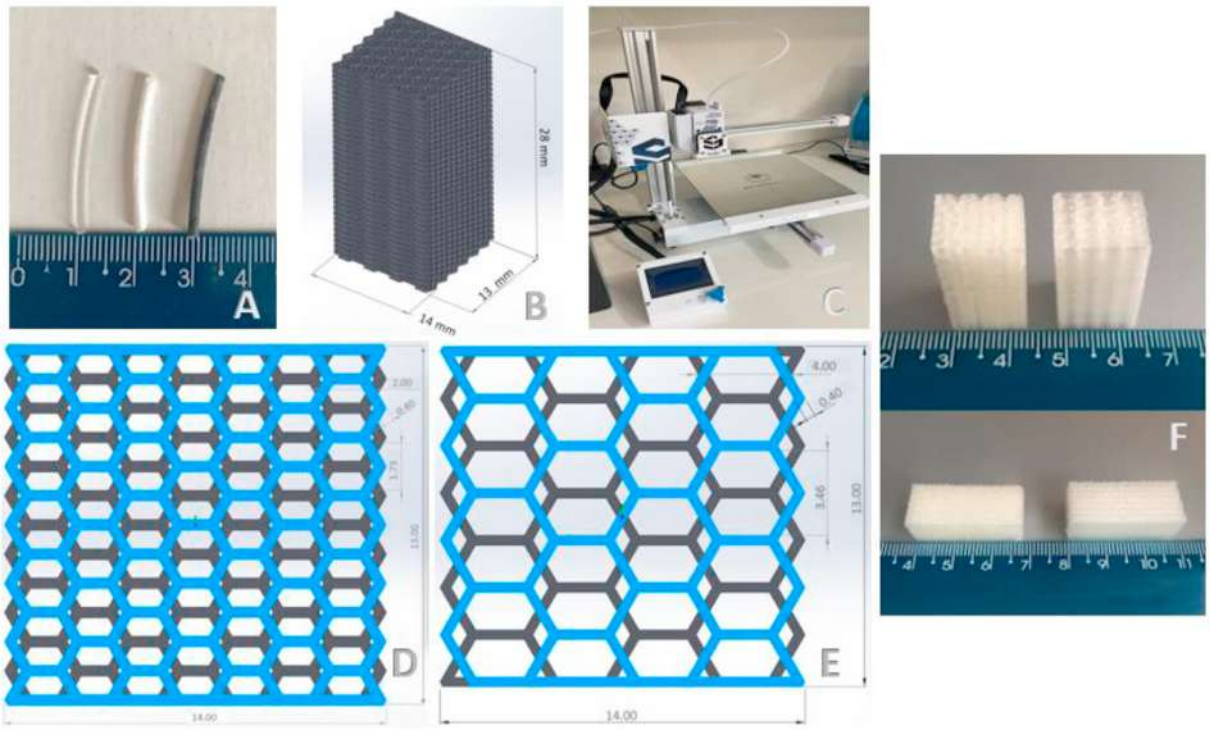

Fig. 4 – Process for obtaining of scaffolds by FDM printing. In A filament produced by FDM in PLA, PLA/BG and PLA/CNT. In B dimensions of the scaffold designed by the modeling software. On C FDM printer. In D and E Layer dimensions with 2 and 4 mm inner spacing. In F scaffold produced by FDM.

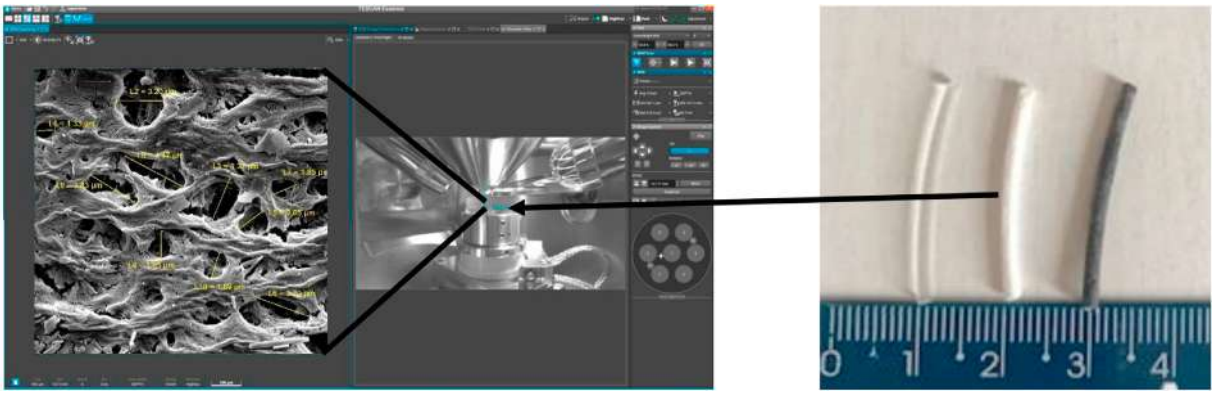

Fig. 5 – Schematic representation of the measurement of the pore size of the filaments used in the printing of scaffolds. Measurement obtained by scanning electronic microscopy, using the Essence Software.

thermal stability, degradation behavior, and percentage of the residual mass of the composite scaffold.

2.5.6. *Compression test*

To determine the mechanical properties by compression, specimens with dimensions of 28x14 × 13 mm were made by 3D printing of the studied materials following the guidelines of ASTM D695-10 [26]. To attend the specifications established by the standard, the specimens were manufactured with dimensions attending the requirement that the height be twice the size of the width. The tests were performed in a universal testing machine model EMIC DL-500 with 500 kgf load cell and 1 mm/min rate. It was performed on PLA, PLA/BG and PLA/CNT scaffolds with 2 and 4 mm of inner spacing between filaments. Several works [27–29] showed the production of scaffolds with smaller inner spacing between the filaments, which justified the choice of the honeycomb geometry in the present work, because with the different intercalated layers, it was possible to obtain smaller inner spacings, between the filaments.

The compressive strength and strain properties were calculated from the load-displacement data. The apparent compressive modulus was based on the slope of the stress–strain curve in the elastic region.

2.5.7. *Cell viability*

The MC3T3 murine calvaria-derived preosteoblast cell line (obtained from the American Type Culture Collection/ATTC, USA) was used to analyze cell viability. Cells were cultured in α-MEM medium supplemented with 10% fetal bovine serum and 1% antibiotic/antimycotic solution (all from Gibco, USA). Twenty-four hours before cultivation on the scaffolds, the cells were maintained in a nutritionally deficient condition (culture medium without the addition of fetal bovine serum) to keep all cells in the same cell cycle phase. Cell viability was assessed using the Alamar Blue assay, a ready-to-use resazurin-based solution (a non-toxic compound that is cell permeable and non-fluorescent blue in color) that functions as an indicator of cell health. Upon entering metabolically active cells, the dye is reduced to resorufin, a highly fluorescent red-colored compound that increases the overall fluorescence and color of the media surrounding cells, which allows the assessment of viability without the need to detach the cells from the scaffolds or lyse them for evaluation.

MC3T3 cells were grown on the PLA, PLA/BG and PLA/CNT scaffold samples of 2 and 4 mm inner spacing, between filaments, impregnated with BG on the surface in 24-well plates at a density of 1×10^4 cells per well. Cells cultured on a polystyrene plastic surface compounded the control group. Two independent experiments were performed in sextuplicate ($n = 6$). After the experimental times of 24, 48 and 72 h, the medium was removed from the wells and the cells were incubated with 30 μL of Alamar Blue (Invitrogen, USA) and 270 μL of α-MEM medium under regular culture conditions. After 4 h, the absorbances of the solution were determined using a microplate reader (at 570 nm for the reduced form and 600 nm for the oxidized form) and the percentage reduction of Alamar Blue in each sample was calculated using the equation provided by the manufacturer.

2.5.8. *Statistical analysis*

Statistical validation of the data was performed using the analysis of variance test (ANOVA), with 95% confidence interval ($p < 0.05$). Mean values were compared using Tukey's test.

3. Results and discussion

3.1. *Characterization of the bioglass synthesized by sol-gel*

Fig. 6A shows the X-ray diffractogram of the bioglass. The diffractometric pattern shows the peaks of the sodium calcium silicate phase (Na_2CaSiO_4) as the majority phase. In Fig. 6B, in the FTIR spectrum of the bioglass, the vibrations of the silicon-oxygen bonds are observed; the vibrations of the phosphate group and the vibrations of carbon-oxygen. In turn, micrographs can be observed in Fig. 6C and D that show agglomerates of variable sizes with pore formation.

The Na_2CaSiO_4 phase found in this study has a high capacity to induce apatite formation as also reported by Zhao et al. [30] and Bellucci et al. [31] when they synthesized bioglass via sol-gel. In addition, another bioactive calcium silicate

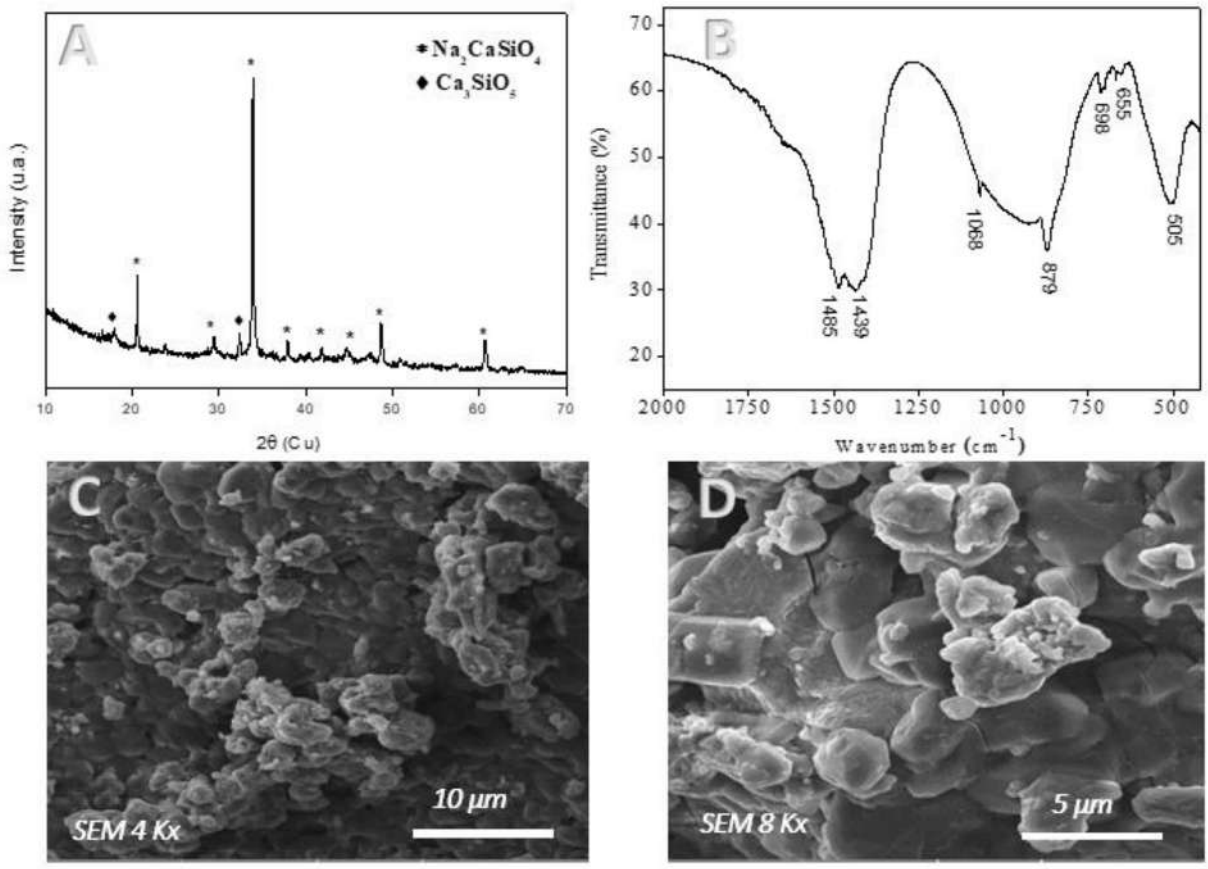

Fig. 6 – Microstructural characterization of bioglass powder synthesized by sol-gel. XRD in A, FTIR in B and Micrographs in C and D.

phase (Ca_3SiO_5) was also found in the present work and reported by Refs. [21,32], being responsible for favoring the formation of hydroxyapatite-deficient crystals that stimulate cell growth, biocompatibility and bioactivity, suggesting that the presence of this phase enhances the application of bioglass in the bone implant area.

As for the FTIR results of the bioglass, in Fig. 6B the following wavelengths were found: 879 and 1068 cm^{-1} associated with the elongation vibrations of silicon with oxygen; 619, 650 and 698 cm^{-1} the vibrations of the phosphate grouping and, at 1440 and 1485 cm^{-1} the vibrations of carbon with oxygen. Similar results were also reported by Bento et al. [33], Vafa et al. [34] and Lucas-Girot et al. [35], on silicon vibrations with oxygen. As for the vibrations of the phosphate grouping and the carbon-oxygen bonds, they were similar with the study by Cacciotti et al. [36], Aguiar et al. [37] and Ben-Arfa et al. [38].

Regarding the micrographs of the bioglass powder, Fig. 6C and D shows agglomerates of variable size with pore formation. Vafa et al. [34] informs that the best bond with the bone tissue is due to the porosity of the material, factors that are beneficial for the circulation of the body fluid and stimulation of cell growth and that are elevated with the use of citric acid in the synthesis of the bioglass [25]. Therefore, the presence of pores in the biomaterial are important attributes for bone repair.

3.2. *Visual appearance, morphological and structural characterization of scaffolds produced by FDM printing*

In Fig. 7, one can observe the hexagonal opening honeycomb geometry in different views. In its interior, interleaved lattices of the hexagonal opening are observed, which produces the decrease of the inner spacing. According to studies [39–41], scaffolds with acute and obtuse angle geometry, characteristic of hexagonal geometry, facilitate angiogenesis and promote good vascularization, attachment, proliferation and cell differentiation, being fundamental for bone regeneration [24].

Fig. 8 shows micrographs of the filaments (A-C) and scaffolds (D, E) with of the 2 and 4 mm inner spacing produced by FDM printing in a view of the top surface of the cut scaffolds. It can be observed that the PLA filament did not present porosity (Fig. 7A), however with the addition of BG and CNT (Fig. 8 B, C) the appearance of pores in the structure of the PLA filament is observed. The average pore size for the filament with BG was equal to 2.43 ± 1.29 μm and for the filament with CNT 5.83 ± 3.20 μm. Serra et al. [42] e Baptista et al. [43] also found a pore diameter similar to the present study. In Fig. 8D, the micrograph of the scaffold with 2 mm inner spacing showed inner distance between filaments and layers ranging between 130 μm and 500 μm. In Fig. 8E, the micrograph of the printed scaffold with 4 mm inner spacing

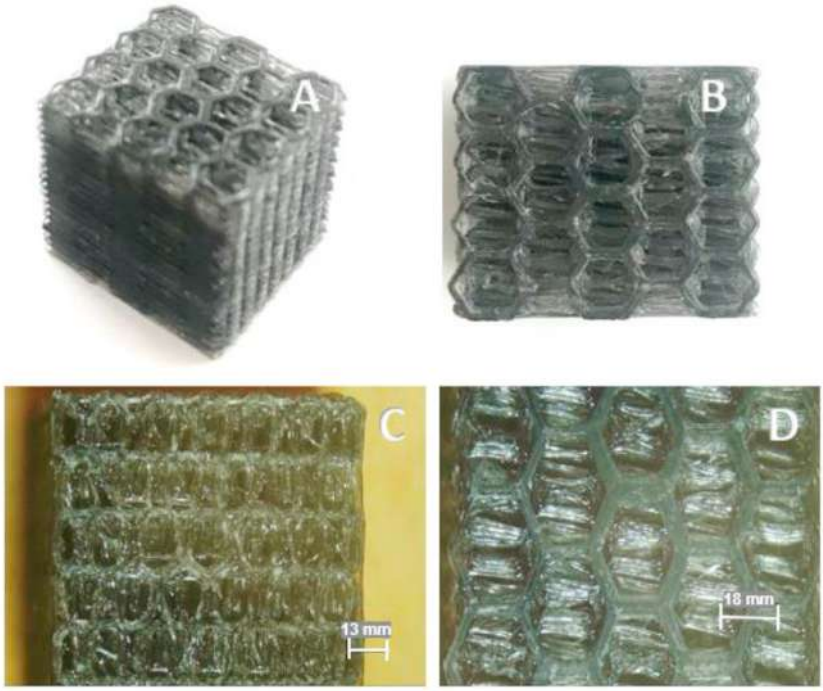

Fig. 7 – Top view obtained by optical microscope with 10x and 0.8x magnification: Top and perspective view of scaffolds in A and B. Macrographs of printed scaffold with 2 mm inner spacing in C and printed scaffold with 4 mm inner spacing in D.

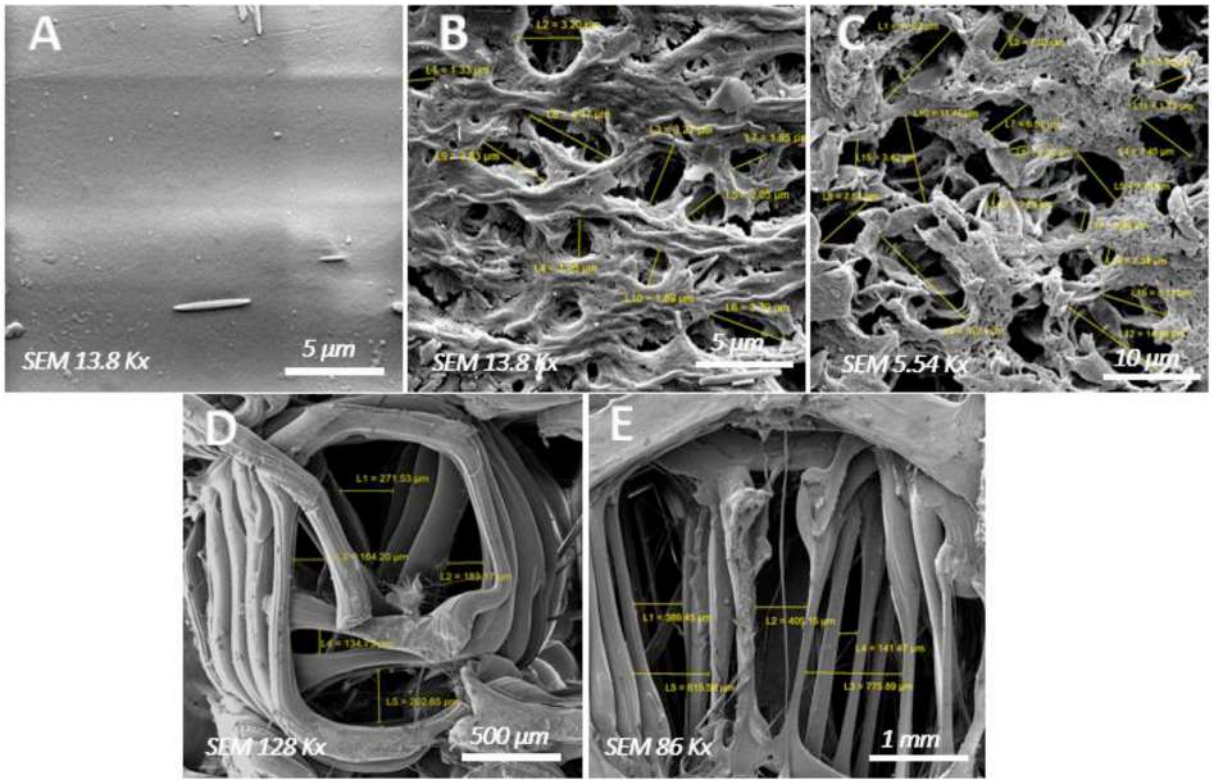

Fig. 8 – Micrographs of filaments and scaffolds. (A) PLA filament; (B) PLA/BG filament; (C) PLA/CNT filament; (D) scaffold with 2 mm of the inner spacing and (E) scaffold with 4 mm of the inner spacing.

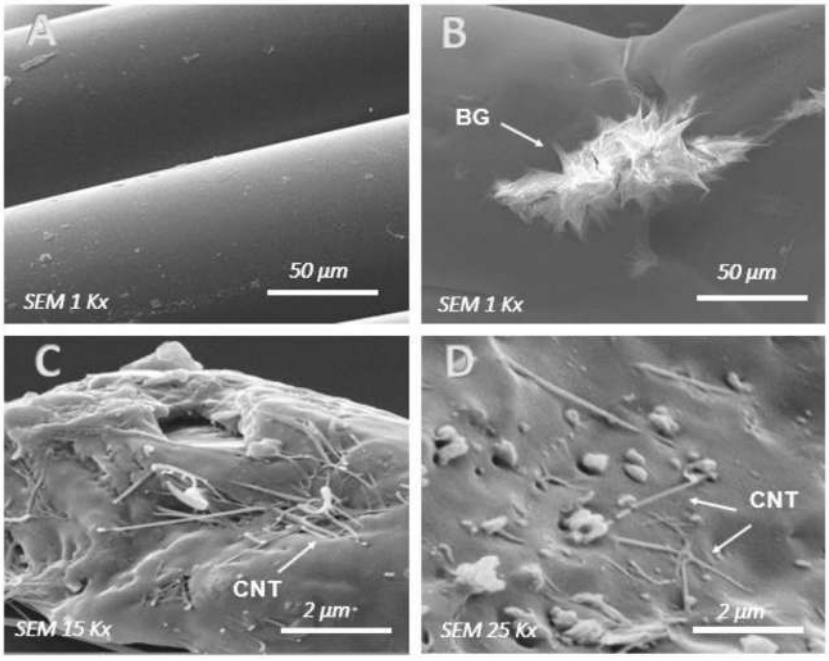

Fig. 9 – Micrographs of the scaffolds before thermal impregnation: PLA in A, PLA/BG in B and PLA/CNT in C and D. Can be observed on the surface of PLA BG in B and CNT in C and D.

showed inner distance between filaments and layers ranging between 150 μm and 800 μm.

In this context, Mohammadi et al. [24] in his study showed that scaffolds with pores of 320–600 μm and hexagonal pore geometry favor better osteogenesis and angiogenesis. Corroborating, Chen et al. [44], pointed out that scaffolds with pores of 500 μm had better cell adhesion, proliferation and osteogenic differentiation.

The morphology of PLA, PLA/BG and PLA/CNT scaffolds can be observed in the micrographs of Fig. 9. Fig. 9A shows a micrograph of the PLA scaffold with a smooth surface, while Fig. 9B shows the presence of bioglass adhered to the polymeric surface and Fig. 9C and D shows the CNT exposed in the region of the scaffold fracture.

Fig. 10 (A, B and C) shows micrographs of the scaffolds after thermal impregnation of the surface with bioglass, and it can be seen that the particles of the bioglass were adhered to the surface of the scaffold. With the particles of bioglass adhered on the surface, it is intended to increase the bioactivity of scaffolds through the bioactive properties of bioglass, since polylactic acid (PLA), despite being considered an important biomaterial for its excellent biocompatibility and degradation in physiological environment, however, has low cellular response [41]. In the study by Canales et al. [41], the bioglass nanoparticles incorporated into PLA by fusion process showed that the incorporation increased the hydrolytic degradation of the polymer improving its degradation process and bioactivity induced by bioglass.

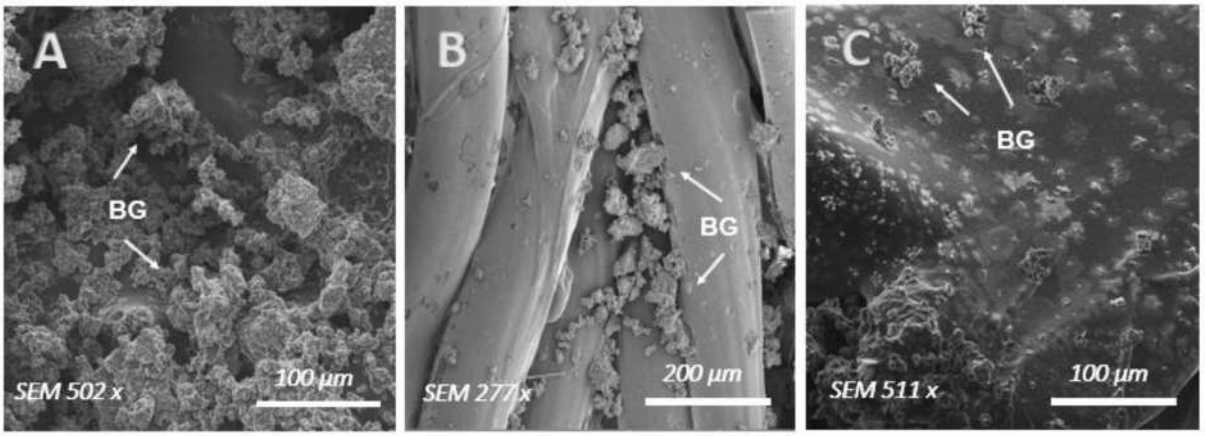

Fig. 10 – Micrographs of the scaffolds after thermal impregnation of the surface with bioglass. PLA in A, PLA/BG in B and PLA/CNT in C.

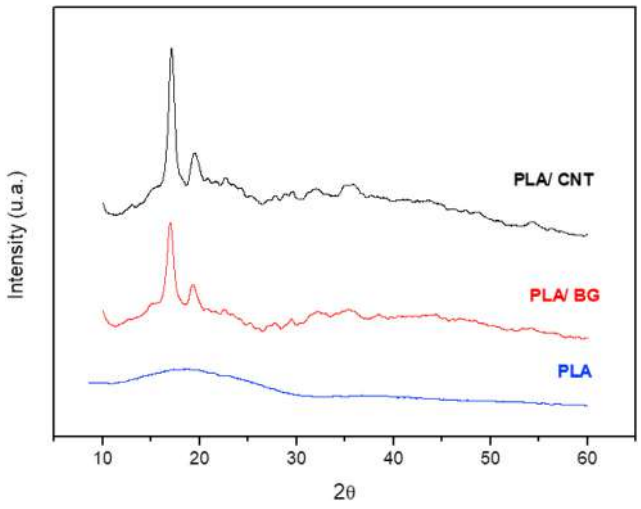

Fig. 11 – XRD diffractogram of PLA, PLA/BG and PLA/CNT filaments.

Fig. 11 shows the diffractograms of the neat PLA, PLA/BG and PLA/CNT filaments after FDM printing. The diffractogram of the neat PLA filament shows only the amorphous halo. In the diffractogram of PLA/BG and PLA/CNT, two peaks are observed corresponding to 2θ equal to 16.5° and 19° related to crystals, being more intense in PLA/CNT. These peaks correspond to the α′ and α crystals, respectively, of PLA that according to Huang et al. [45] is due to the polymer melting that occurs in the extrusion of FDM printing, suggesting that the crystalline behavior of PLA is affected by BG and CNT after 3D printing. And according to Zhou et al. [46] this addition acts as a nucleation site for the growth of PLA crystals.

Fig. 12 shows the Raman spectra of the bioglass, the PLA and PLA/BG scaffolds and the PLA and PLA/BG scaffold after the impregnation of the surface with bioglass, being named PLA Imp BG and PLA/BG Imp BG.

In the Raman spectrum of the bioglass it is possible to observe the vibrations of the typical bands of the Si–O–Si bond, in the range 900–970 cm^{-1} corresponds to the Si-O-NBO (non-point oxygen) stretching and the 1000 to 1100 cm^{-1} to that of asymmetric Si–O–Si stretching [37,47]. Whereas, the bands from 800 to 1000 cm^{-1} are associated with the Si–O–Si bond in the silica tetrahedron with a different number of non-point oxygen (NBO) [31]. Whereas, the vibrational bands at 938 cm^{-1} are characteristic of Si–O–Si stretching and bending modes, the peak at 1069 cm^{-1} is assigned to a bond stretching vibration, in which the bridging oxygen atom moves parallel

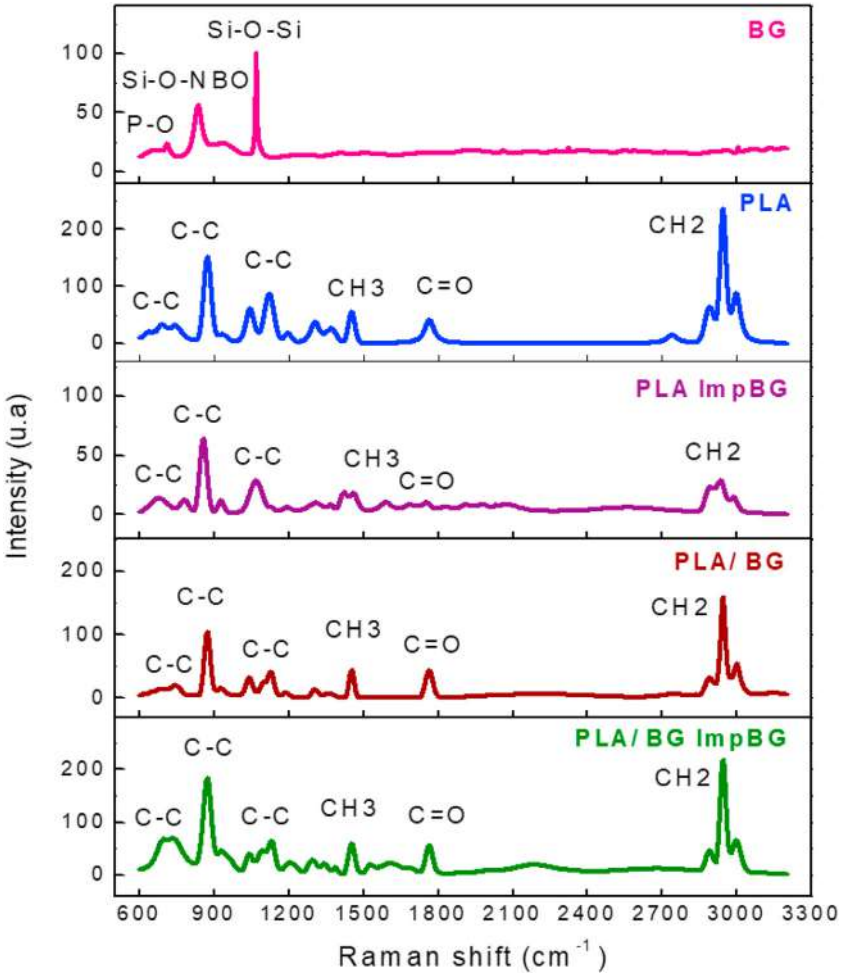

Fig. 12 – Raman spectrum of bioglass and PLA and PLA/BG scaffolds before and after thermal impregnation of the surface with bioglass.

to the Si–Si lines. Whereas, the band around 600 cm^{-1} was assigned to the phosphate (P–O) vibration [48].

The characteristic peaks of PLA were assigned to: 2740, 2891, 2947 and 3000 cm^{-1} which corresponds to the stretching vibration of the CH_2 structural arrangement; 1765 cm^{-1} to the C=O stretching vibration; 1454, 1370, 1306 cm^{-1} to the bending vibration of the CH_3 arrangement; 1196, 1122, 1045, 746, 689 and 632 cm^{-1} to the C–C stretching vibration; 934 cm^{-1} swing vibration with CH_3 and; 873 cm^{-1} to the C–COO stretching vibration of the repetitive unit of the PLA polymer chain [44,49,50].

In Table 1, one can compare the peaks found in the Raman spectra of PLA and PLA impregnated with BG, as well as in Table 2 the peaks found in the spectra of PLA/BG and PLA/BG impregnated with BG with their respective FHWM (width and half-height). Note the characteristic vibration bands of the polymer and the strong interaction with the BG inducing new vibrational modes and generating new bands between 1400 and 2600 cm^{-1}. In addition, the increase in FWHM indicates an increase of functional groups adsorbed on the matrix, thus showing the interaction of the bioglass with the PLA matrix.

Fig. 13 presents the Raman spectrum of the PLA/CNT scaffolds before and after impregnation with BG on the surface, being named PLA/CNT Imp BG. Table 3 shows the peaks found in the respective spectra. The D band at 1333 cm^{-1} and G band at 1594 cm^{-1} were identified, confirming the existence of the carbon nanotubes in the 3D printed material. This result was similar to that presented by Vidakis et al. [51] with the fabrication of PLA/CNT nanocomposites by 3D printing. Ivanov et al. [52] in turn observed that the bands at 2890-3000 cm^{-1} of the polymer matrix decreased with the presence of the carbon nanotubes. The Raman spectrum of PLA/CNT Imp BG scaffolds showed decreased intensity of the peaks related to the D (1334 cm^{-1}), G (1594 cm^{-1}) and 2D (2661 cm^{-1}) bands, indicative of carbon nanotubes. The degree of defects in the graphitic structure is characterized by the ratio between the intensities of the D and G bands (ID/IG), the lower the value of the ratio, the lower the amount of defects in the carbon structure. Thus, the ratio values (ID/IG) for PLA/CNT were 2.2 and for PLA/CNT Imp BG was 1.6. Also, the increase of the FHWM of the D-band was observed being indicative of the increase of defects or functionalization in the CNTs and also the intensity of the D-band higher than the G-band confirming also the defects of functionality.

3.3. *Thermogravimetric analysis and its derivative (TGA/DTG)*

The results of thermogravimetric analysis (TGA) and corresponding differential thermogravimetric analysis (DTG) (Fig. 14) provides data for the thermal and oxidative stability of the PLA/CNT Imp BG composite sample and the approximate residual mass percentage of CNT and BG incorporated into the polymer substrate. The PLA/CNT Imp BG composite sample showed decomposition at 266 °C with a DTG peak of 315 °C.

The TGA curve shows two mass losses after the temperature increase. The initial mass of the composite sample was 5.48 mg and the losses appeared in the temperature ranges of 100–163 °C and 266–347 °C. The first mass loss between 100

Table 1 – Deconvolutions of the main spectrum Raman of PLA scaffolds and PLA impregnated with bioglass (BG).

Deconvolutions of PLA cm^{-1} peaks	FWHM PLA cm^{-1}	Deconvolutions of PLA Imp BG peaks cm^{-1}	FWHM PLA Imp BG cm^{-1}
632	61.29	–	–
689	47.45	677	92.11
746	63.81	780	43.68
873	35.57	857	34.12
934	44.86	927	31.66
1045	39.67	1068	59.45
1122	45.04	–	–
1196	34.50	1191	46.43
1306	44.18	1308	80.90
1370	46.78	1368	23.03
–	–	1419	33.20
1454	31.25	1460	41.66
–	–	1588	65.43
–	–	1685	61.60
1765	45.87	1752	50.89
–	–	1830	57.41
–	–	1910	64.85
–	–	1976	47.29
–	–	2030	13.66
–	–	2074	141.43
–	–	2564	418.13
2740	51.34	–	–
2891	41.83	2891	40.75
2947	28.74	2936	41.20
3000	39.80	2989	38.01

Table 2 – Deconvolutions of the peaks of the Raman spectrum of PLA/BG and PLA/BG scaffolds impregnated with bioglass (BG).

Deconvolutions PLA/BG cm^{-1} peaks	FWHM PLA/BG cm^{-1}	Deconvolutions PLA/BG Imp BG cm^{-1} peaks	FWHM PLA/BG Imp BG cm^{-1}
691	131.56	689	56.70
748	39.99	740	90.75
873	28.69	873	31.53
926	47.39	955	56.77
1040	33.10	1040	32.55
1096	29.40	1091	43.52
1128	29.99	1132	32.94
1187	37.34	1206	58.41
1303	30.99	1294	40.33
1360	55.42	1343	20.03
-	–	1385	23.52
1454	27.61	1454	30.99
-	–	1526	31.91
-	–	1608	111.98
-	–	1696	38.10
1765	34.47	1765	33.25
2206	460.93	2183	211.63
		2684	401.89
2746	110.17	–	–
2835	17.80	–	–
2889	38.17	2891	36.87
2947	23.59	2947	27.62
3002	35.18	2999	43.44
3153	137.43	–	–

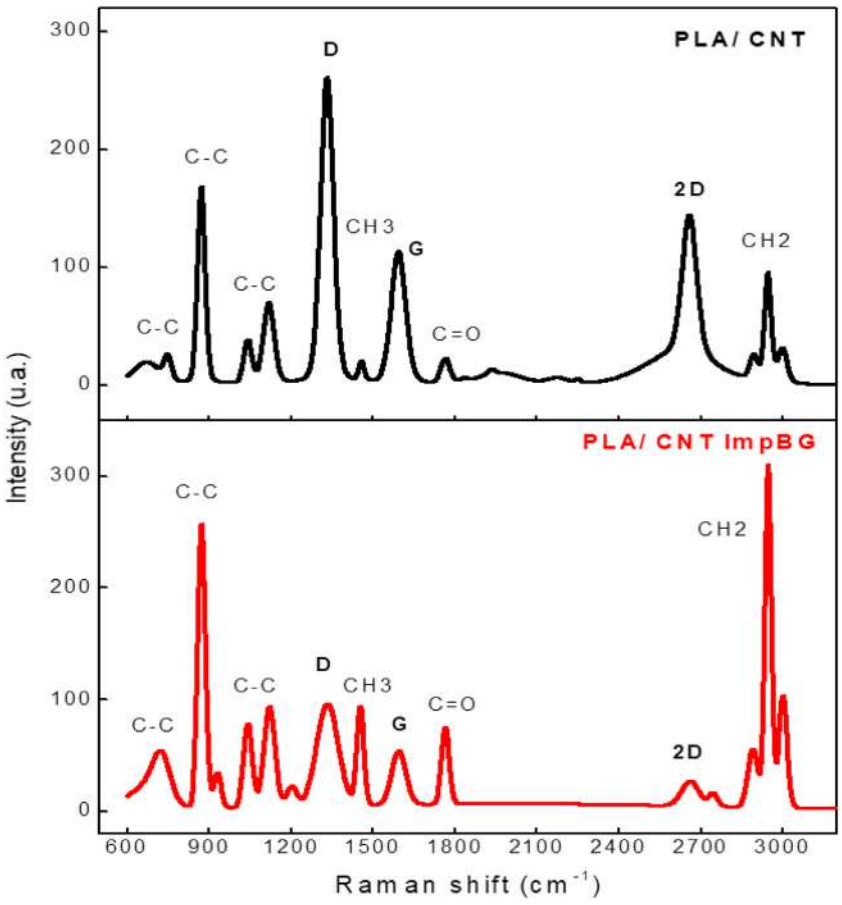

Fig. 13 – Raman spectrum of PLA/CNT scaffold before and after thermal impregnation of the surface with bioglass.

Table 3 – Deconvolutions of the Raman spectrum peaks of PLA/CNT scaffolds and PLA/CNT impregnated with bioglass (BG).

Deconvolutions of peaks PLA/CNT cm^{-1}	FWHM PLA/CNT cm^{-1}	Deconvolutions of PLA/CNT Imp BG cm^{-1} peaks	FWHM PLA/CNT Imp BG cm^{-1}
669	114.48	671	152.99
748	34.08	726	73.27
873	32.76	873	33.15
-	–	931	31.37
1042	34.59	1042	37.55
1119	46.69	1122	46.63
-	–	1202	42.07
1333	55.29	1334	92.17
1458	24.39	1454	30.00
1594	62.42	1594	87.64
1765	39.39	1765	32.85
1963	187.25	–	–
2175	89.70	–	–
2622	304.61	–	–
2660	63.05	2661	73.57
-	–	2745	35.65
2894	35.57	2892	43.53
2947	29.11	2948	27.52
3000	39.28	3001	35.58

and 163 °C is observed to be approximately 1.058% (0.058 mg) which can be attributed to adsorbed water. The second mass loss occurs between 266 and 347 °C, being quite significant with degradation and loss of 94.82% which corresponds to 5.19 mg of mass. The peak of the DTG curve of 315 °C indicates

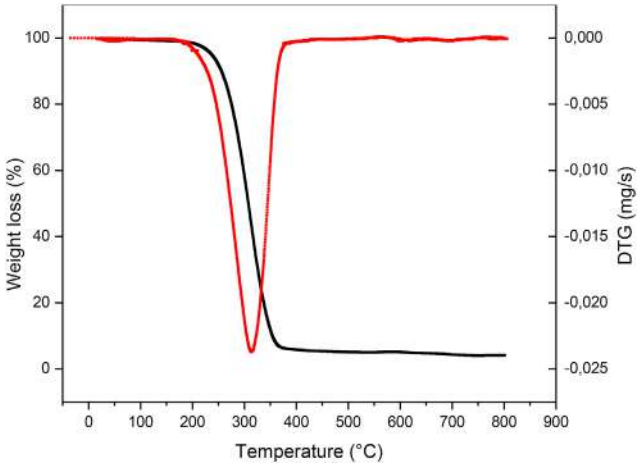

Fig. 14 – TGA and DTG curves of the PLA/CNT imp BG. TGA/DTG provides data for the thermal and oxidative stability of the PLA/CNT Imp BG composite sample and the approximate residual mass percentage of CNT and BG incorporated into the polymer substrate.

the maximum temperature of degradation, being attributed to the degradation of the polymer. At the end of the degradation, it can be seen that all polymeric material was decomposed having a residue of 5.2% mass corresponding to 0.22 mg that is not degraded at the maximum temperature analyzed, suggesting to be CNT and BG.

Similar behavior was found in the studies of Abeer et al. [53] where the pure PLA scaffold showed thermal decomposition of the polymer from 300 to 370 °C and almost complete mass loss (99.15%), while in the PLA/BG scaffold the thermal decomposition was from 230 to 300 °C.

3.4. *Compression test*

For the compression and cell viability tests it was used in the nomenclature PLA, PLA/BG and PLA/CNT the numbers 2 and 4 meaning the inner spacing of the scaffolds.

Fig. 15A shows the graph of the compressive strength in relation to the type of material analyzed. Among the scaffold models with 2 mm of the inner spacing, PLA presented the highest compressive strength corresponding to 14.88 ± 2.35 MPa. Among the 4 mm of the inner spacing scaffold models, the PLA/NTC presented the highest compressive strength value of 9.76 ± 6.28 MPa. Fig. 15B shows the behavior of the scaffolds in relation to the deformation and it can be seen that the scaffolds with the highest deformation were PLA2 with 0.16 ± 0.02 (%) and PLA/BG4 corresponding to 0.24 ± 0.05 (%). Fig. 15C shows the graph of the average apparent compressive modulus and it can be seen that the scaffolds with the highest stiffness were PLA/CNT2 with 0.58 ± 0.36 GPa and PLA4 with 0.36 ± 0.25 GPa. The size of the inner spacing in the scaffold structure may directly influence the mechanical behavior and, as seen in Fig. 8, the openings varied between 130 μm and 500 μm, for scaffold produced

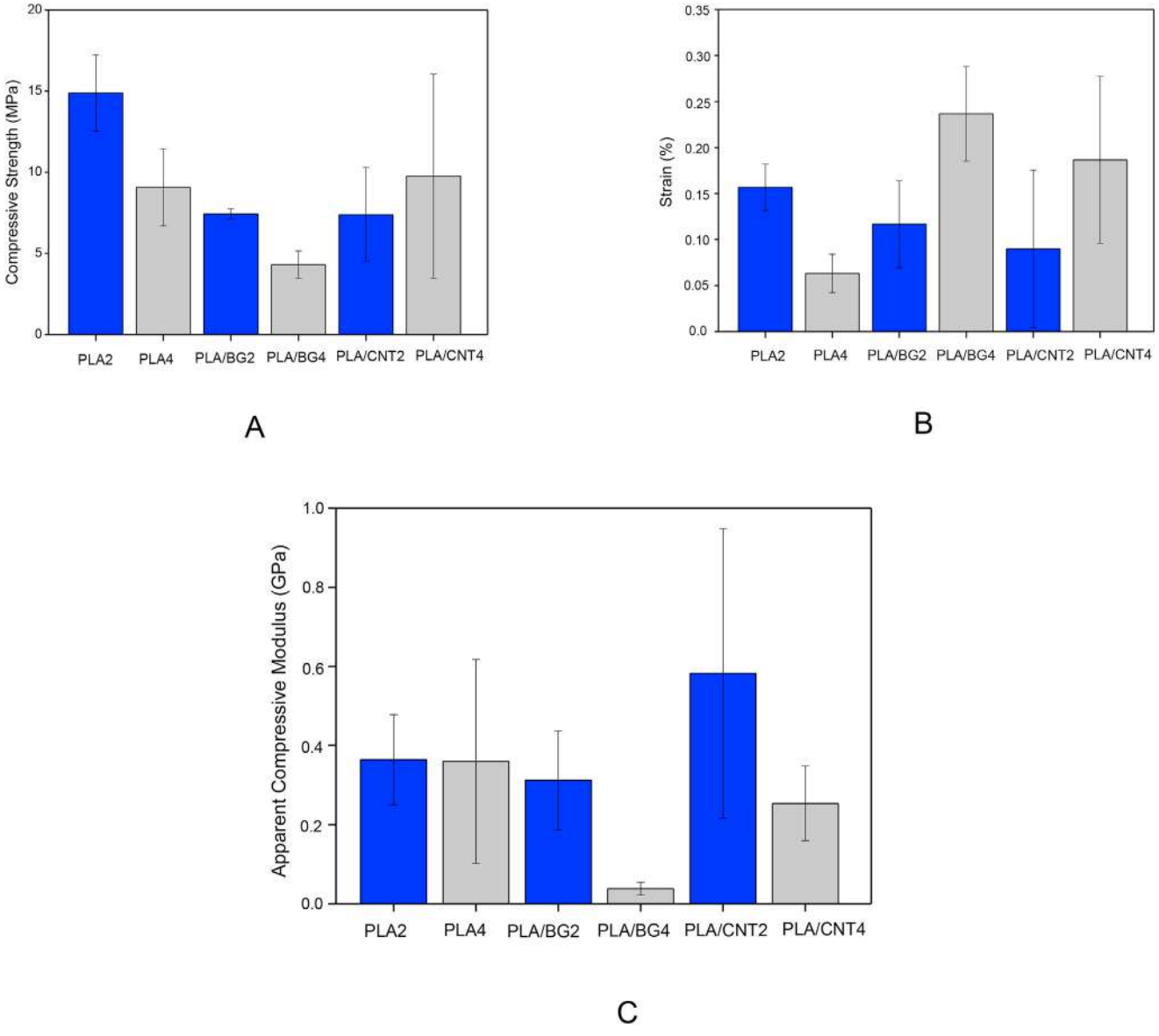

Fig. 15 – Mechanical properties obtained from uniaxial compression tests. The data represent the average values and the standard deviation of the evaluated mechanical properties. Compressive Strength at A, Strain at B and Apparent Compressive Modulus at C.

with 2 mm of the inner spacing, and 150 μm and 800 μm for scaffold with 4 mm of the inner spacing. Another factor that may explain the decrease in compressive strength of PLA/BG and PLA/CNT scaffolds is that the insertion of these components into PLA caused an increase in porosity in the filament, as can be seen in Fig. 8 (A-C). Despite the average pore size, in the filaments, being smaller in PLA/BG scaffolds, the compressive strength in these materials was lower than in PLA/CNT, suggesting that, in spite of increasing the pore size in PLA, insertion of CNT led to a slight increase in compressive strength due to its intrinsic properties. The same standard was found by Corcione et al. [54] when hydroxyapatite microspheres were incorporated into PLA in the production of scaffolds for use in bone regeneration. The authors attributed the decrease in compressive strength to the incorporation of hydroxyapatite in the PLA structure. Serra et al. [8] also obtained similar results to the present study and the authors state that, despite the strength being lower than that of the trabecular bone the scaffold was able to act as templates during the first phases of bone regeneration. Baptista et al. [55] found better values for the mechanical performance of PLA scaffolds printed via 3 d-printing with porosity and geometry variation. The authors concluded that staggered scaffolds showed a greater reduction in open porosity and an increase in mechanical properties when compared to the other configurations. Baptista and Guedes [56] also obtained PLA scaffolds with excellent mechanical performance when evaluating the variation in geometry and porosity and concluded that this material may be applied as a bone substitute.

The statistical analysis of the mechanical properties in compression is presented in Table 4. For compressive strength, one can see that for p-*value* of 0.028695, the calculated F (3.72) is higher than the critical F value (3.10), as for strain, the p-*value* is 0.035863 and the calculated F (3.47) is higher than the critical F value (3.10). Thus, the hypothesis that the averages of the presented specimens are equal is rejected at 95% confidence level. Due to the ANOVA results, Tukey's test was necessary to investigate whether the bioglass and carbon nanotubes were more effective in causing significant changes in the mechanical properties of the scaffolds and for minimum significant difference (M.S.D) of 6.878504 it was observed that PLA/BG2, PLA/BG4 and PLA/CNT2 scaffolds present statistical differences regarding compressive strength and PLA4, PLA/BG4 and PLA/CNT2 present statistical differences regarding deformation do M.S.D. of 0.130193. For apparent compressive modulus, the p-*value* was 0.035863 and the calculated F (2.36) was lower than the critical value F (3.10) and this result reveals that there is no statistical difference between the scaffolds.

Thus, it can be inferred that the inclusion of bioglass and carbon nanotubes in the PLA matrix caused changes in the mechanical properties in compressive strength and strain of the scaffolds. On the other hand, no significant difference was found in the apparent compressive modulus values between the PLA matrix and the composites with bioglass and carbon nanotubes. The results were compatible with trabecular bone, such as present in vertebrae, skull and joints, which has compressive strength of 2–20 MPa and apparent compressive modulus of 0.1–2.0 GPa [57].

3.5. *Cell viability*

The reduction of Alamar Blue® was evaluated at three different incubation times, the values being obtained from the absorbance readings at 24 h, 48 h and 72 h.

Fig. 16 presents the data from the Alamar Blue assay showing that all groups of scaffolds exhibited lower cell proliferation compared to the control group. Among the scaffold groups analyzed, the 4 mm of the inner spacing scaffolds showed better cell proliferation. Regarding the time, the scaffolds, in 24 h of the PLA/BG4 group was the one that presented the best cell proliferation with 32.82 ± 0.90 (%). In 48 h, the same group also presented the best result with 32.53 ± 16.78 (%). In 72 h, the PLA4 group showed the highest cell proliferation with 38.53 ± 24.39 (%).

Table 4 – Analysis of single factor variance for compression assay of PLA, PLA/BG and PLA/CNT scaffolds with 2 and 4 mm diameter produced by FDM printing. Compressive Strength: p-*value* - 0.028695 and M.S.D - 6.878504; Strain: p-*value* - 0.035863 and M.S.D - 0.130193; Apparent Compressive Modulus: p-*value* - 0.035863.

Compressive Strength (MPa)						
Source	Sum of Squares	Degrees of Freedom	Mean of Squares	F (calculated)	F critical	*p*-value
Source	Sum of Squares	Degrees of Freedom	Mean of Squares	F (calculated)	F critical	*p*-value
Between the groups	186,1782	5	37,23564	3,728483	3,105875	0,028695
Inside the group	119,8417	12	9,986806			
Total	306,0198	17				
Strain						
Source	Sum of Squares	Degrees of Freedom	Mean of Squares	F (calculated)	F critical	*p*-value
Between the groups	0,062117	5	0,012423	3,47236	3,105875	0,035863
Inside the group	0,042933	12	0,003578			
Total	0,10505	17				
Apparent Compressive Modulus (GPa)						
Source	Sum of Squares	Degrees of Freedom	Mean of Squares	F (calculated)	F critical	*p*-value
Between the groups	0,469103	5	0,093821	2,363193	3,105875	0,103199
Inside the group	0,476409	12	0,039701			
Total	0,945512	17				

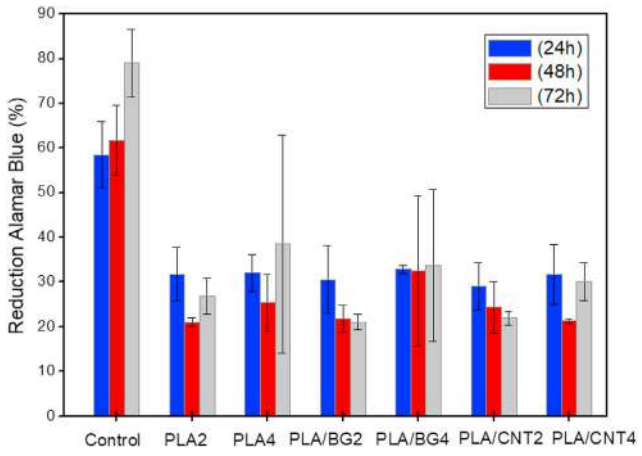

Fig. 16 – Reduction of Alamar Blue in different intervals (24, 48 and 72 h). The data represent the mean ± standard deviation of the mean cellular viability sample in fluorescence.

The two-way ANOVA statistical analysis was applied and reveals that between the materials and the control, the calculated F (25.28) is higher than the critical F value (2.32), thus requiring the application of Tukey's test. It can be inferred that, between the materials and the control, they are statistically different (M.S.D. of 22.37). The analysis between the samples of the study materials, the double factorial ANOVA statistical results point out that there is no significant difference between these groups, because the calculated F (3.06) is inside the critical F value (3.21).

Some limitations could have influenced the difference in the results of the Alamar blue assay between the control group and the scaffolds tested. The first is that the hydrophilicity of PLA can be an obstacle to cell viability due to its degradation with acidic products [58]. The second is that in the control group, the cells were seeded on a polystyrene surface, which has been considered the gold standard surface for adherent cell cultures due to its biocompatibility and physical properties [59,60], while in the tested groups the cells need to overcome the possible limitations related to the physical properties of the microenvironment so that they can adhere and then proliferate. In a general analysis of scaffolds groups, after a drop in cell growth at 24 and 48 h, it is observed that there was cell growth at 72 h. As the study covered only three days, the ability of the cells to overcome these eventual integration difficulties with the scaffold surfaces may not have been adequately detected.

Thus, it is noted that the scaffolds produced presented themselves as potential materials for the development of artificial structures with application as bone substitutes and can be an alternative for regenerative medicine and for tissue engineering.

4. Conclusions

This study demonstrated that PLA, PLA/BG and PLA/CNT scaffolds can be produced as 3D printed structures by FDM technique with a controlled geometric structure with interleaved hexagonal honeycomb pores, with good reproducibility and precision, fundamental characteristics for the fabrication of customized biomaterials, and with mechanical properties in compression similar to trabecular bone. The SEM analysis revealed the porous microstructure in the filaments of the scaffolds. In the Raman structural characterization, it was possible to identify the interactive vibrational behavior of the structural arrangements of the materials in this study and the emergence of new peaks, not reported in the literature, demonstrated the interaction of bioglass and carbon nanotubes with the polymer matrix. Furthermore, the good thermal stability of the PLA/CNT Imp BG composite. In the cell viability analysis, the results were lower than the control group, however, at 72 h there was greater cell proliferation among the scaffolds. Thus, the results showed that the three-dimensional scaffold of hexagonal honeycomb geometry of PLA, BG and CNT has potential for applications in biomaterials, but needs further studies in the area. Although the study with scaffolds shows interesting data for using 3D printed composites for bone repair in vertebrae, ribs, skull and joint bones, the application for future implants remains limited regarding biocompatibility for osteogenic integration, regardless of the type of scaffold generated by 3D printing.

Special thanks to: Higher Education Improvement Coordination. Pro-Rector of Research and Graduate Studies of the Federal University of Pará; Laboratory of Mineral Characterization; Laboratory of Modeling, Simulation and System Control; Laboratory of Nanomanipulation, Laboratory of Vibrational Spectrometry and High Pressures, Amazonian Oils and Eco Composites Laboratory of UFPA, Laboratory of Cell Culture of the Biosciences Center of the Federal University of Rio Grande do Norte and Advanced Materials Laboratory at State University of Norte Fluminense.

Declaration of competing interest

The authors declare that they have no known competing financial interests or personal relationships that could have appeared to influence the work reported in this paper.

REFERENCES

[1] Heath DE, Kang GCW, Cao Y, Poon YF, Chan V, Chan-park MB. Biomaterials patterned with discontinuous microwalls for vascular smooth muscle cell culture: biodegradable small diameter vascular grafts and stable cell culture substrates. J Biomater Sci Polym Ed 2016;27:1477–94.

[2] Eivazzadeh-Keihan R, Maleki A, Guardia M, Bani MS, Chenab KK, Pashazadeh-Panahi P, et al. Carbon based nanomaterials for tissue engineering of bone: building new bone on small black scaffolds: a review. J Adv Res 2019;18:185–201.

[3] Dasgupta S, Maji K, Nandi SK. Investigating the mechanical, physiochemical and osteogenic properties in gelatin-chitosan-bioactive nanoceramic composite scaffolds for bone tissue regeneration: in vitro and in vivo. Mater Sci Eng C 2019;94:713–28.

[4] Feng P, Jia J, Liu M, Peng S, Zhao Z, Shuai C. Degradation mechanisms and acceleration strategies of poly (lactic acid) scaffold for bone regeneration. Mater Des 2021;210:110066.
[5] Barbeck M, Serra T, Booms P, Stojanovic S, Najman S, Engel E, et al. Analysis of the in vitro degradation and the in vivo tissue response to bi-layered 3D-printed scaffolds combining PLA and biphasic PLA/bioglass components – guidance of the inflammatory response as basis for osteochondral regeneration. Bioact Mater 2017;2:208–23.
[6] Khosravani MR, Reinicke T. Effects of raster layup and printing speed on strength of 3D-printed structural components. Procedia Struct Integr 2020;28:720–5.
[7] Korpela J, Kokkari A, Korhonen H, Malin M, Närhi T, Seppälä J. Biodegradable and bioactive porous scaffold structures prepared using fused deposition modeling. J Biomed Mater Res B Appl Biomater 2013;101:610–9.
[8] Serra IR, Fradique R, Vallejo MCS, Correia TR, Miguel SP, Correia IJ. Production and characterization of chitosan/gelatin/β-TCP scaffolds for improved bone tissue regeneration Materials. Science and Engineering C 2015;55:592–604.
[9] Lee CS, Hwang HS, Kim S, Fan F, Aghaloo T, Lee M. Inspired by nature: facile design of nanoclay–organic hydrogel bone sealant with multifunctional properties for robust bone regeneration. Adv Funct Mater 2020;30:2003717.
[10] Popescu RA, Tabaran FA, Bogdan S, Farcasanu A, Purdoiu R, Magyari K, Vulpoi A, Dreanca A, Sevastre B, Simon S, Papuc I, Baia L. Bone regeneration response in an experimental long bone defect orthotopically implanted with alginate-pullulan-glass-ceramic composite scaffolds. J Biomed Mater Res 2020;108B:1129–40.
[11] Gregor A, Filová E, Novák M, Kronek J, Chlup H, Buzgo M, et al. Designing of PLA scaffolds for bone tissue replacement fabricated by ordinary commercial 3D printer. J Biol Eng 2017;11:31.
[12] Wurm M, Möst T, Bergauer B, Rietzel D, Neukam FW, Cifuentes SC, et al. In-vitro evaluation of Polylactic acid (PLA) manufactured by fused deposition modeling. J Biol Eng 2017;11:1–9.
[13] Zou L, Zhang Y, Liu X, Chen J, Zhang Q. Biomimetic mineralization on natural and synthetic polymers to prepare hybrid scaffolds for bone tissue engineering. Colloids Surf B Biointerfaces 2019;178:222–9.
[14] Szcześ A, Hołysz L, Chibowski E. Synthesis of hydroxyapatite for biomedical applications. Adv Colloid Interface Sci 2017;249:321–30.
[15] Arcos D, Vallet-Regí M. Substituted hydroxyapatite coatings of bone implants. J Mater Chem B 2020;8:1781–800.
[16] Baino F, Fiorilli S, Vitale-Brovarone C. Bioactive glass-based materials with hierarchical porosity for medical applications: review of recent advances. Acta Biomater 2016;42:18–32.
[17] de Souza LPL, Lopes JH, Ferreira FV, Martin RA, Bertran CA, Camilli JA. Evaluation of effectiveness of 45S5 bioglass doped with niobium for repairing critical-sized bone defect in in vitro and in vivo models. J Biomed Mater Res 2020;108A:446–57.
[18] Owens GJ, Singh RK, Foroutan F, Alqaysi M, Han CM, Mahapatra C, et al. Sol–gel based materials for biomedical applications. Prog Mater Sci 2016;77:1–79.
[19] Siqueira RL, Zanotto ED. Biosilicato®: histórico de uma vitrocerâmica brasileira de elevada bioatividade. Quím Nova 2011;34:1231–41.
[20] Bianco A, Kostarelos K, Prato M. Making carbon nanotubes biocompatible and biodegradable. Chemical Communications journal 2011;47:10183–8.
[21] Yang L, Zhang L, Webster TJ. Carbon nanostructures for orthopedic medical applications. Nanomedicine 2011;6:1231–44.
[22] Hamilton RF, Wu Z, Mitra S, Holian A. The effects of varying degree of MWCNT carboxylation on bioactivity in various in vivo and in vitro exposure models. Int J Mol Sci 2018;19:354.
[23] Touri R, Moztarzadeh F, Sadeghian Z, Bizari D, Tahriri M, Mozafari M. The use of carbon nanotubes to reinforce 45S5 bioglass-based scaffolds for tissue engineering applications. BioMed Res Int 2013;1:1–8.
[24] Mohammadi H, Sepantafar M, Muhamad N, Sulong AB. How does scaffold porosity conduct bone tissue regeneration? Adv Eng Mater 2021;23:2100463.
[25] Faure J, Drevet R, Lemelle A, Jaber NB, Tara A, Btaouri HE, et al. A new sol–gel synthesis of 45S5 bioactive glass using an organic acid as catalyst. Mater Sci Eng C 2015;47:407–12.
[26] ASTM D695-10. Standard test method for compressive properties of rigid plastics compression tests. West Conshohocken, PA, USA: ASTM International; April 1, 2010.
[27] Alksne M, Kalvaityte M, Simoliunas E, Rinkunaite I, Gendviliene I, Locs J, Rutkunas V, Bukelskiene V. In vitro comparison of 3D printed polylactic acid/hydroxyapatite and polylactic acid/bioglass composite scaffolds: insights into materials for bone regeneration. J Mech Behav Biomed Mater 2020;104:103641.
[28] Pierantozzi D, Scalzone A, Jindal S, Stīpniece L, Šalma-Ancāne K, Dalgarno K, Gentile P, Mancuso E. 3D printed Sr-containing composite scaffolds: effect of structural design and material formulation towards new strategies for bone tissue engineering. Compos Sci Technol 2020;191:108069.
[29] Distler T, Fournier N, Grünewald A, Polley C, Seitz H, Detsch R, Boccaccini AR. Polymer-bioactive glass composite filaments for 3D scaffold manufacturing by fused deposition modeling: fabrication and characterization. Front Bioeng Biotechnol 2020;8:552.
[30] Zhao Y, Ning C, Chang J. Sol–gel synthesis of Na2CaSiO4 and its in vitro biological behaviors. J Sol Gel Sci Technol 2009;52:69–74.
[31] Bellucci D, Sola A, Salvatori R, Anesi A, Chiarini L, Cannillo V. Sol–gel derived bioactive glasses with low tendency to crystallize: synthesis, post-sintering bioactivity and possible application for the production of porous scaffolds. Mater Sci Eng C 2014;43:573–86.
[32] Fu T, Alajmi Z, Shen Y, Wang L, Yang S, Zhang M. Sol-gel preparation and properties of Ag-containing bioactive glass films on titanium. Int J Appl Ceram Technol 2017;14:1117–24.
[33] Bento R, Gaddam A, Ferreira JMF. Sol–gel synthesis and characterization of a quaternary bioglass for bone regeneration and tissue. Materials 2021;14:4515.
[34] Vafa E, Bazargan-Lari R, Bahrololoom ME. Synthesis of 45S5 bioactive glass-ceramic using the sol-gel method, catalyzed by low concentration acetic acid extracted from homemade vinegar. J Mater Res Technol 2021;10:1427–36.
[35] Lucas-Girot A, Mezahi FZ, Mami M, Oudadesse H, Harabi A, Floch MLM. Sol–gel synthesis of a new composition of bioactive glass in the quaternary system SiO2–CaO–Na2O–P2O5: comparison with melting method. J Non-Cryst Solids 2011;357:3322–7.
[36] Cacciotti I, Lombardi M, Bianco A, Ravaglioli A, Montanaro L. Sol–gel derived 45S5 bioglass: synthesis, microstructural evolution and thermal behavior. J Mater Sci Mater Med 2012;23:1849–66.
[37] Aguiar H, Serra J, González P, León B. Structural study of sol–gel silicate glasses by IR and Raman spectroscopies. J Non-Cryst Solids 2009;355:475–80.
[38] Ben-Arfa BAE, Salvado IMM, Ferreira JMF. Pullar RC Enhanced bioactivity of a rapidly-dried sol-gel derived quaternary bioglass. Mater Sci Eng C 2018;91:36–43.
[39] Diez-Escudero A, Andersson B, Persson C, Hailer NP. Hexagonal pore geometry and the presence of

hydroxyapatite enhance deposition of mineralized bone matrix on additively manufactured polylactic acid scaffolds. Mater Sci Eng C 2021;125:112091.
[40] Abbasi N, Hamlet S, Love RM, Nguyen N. Porous scaffolds for bone regeneration. J Sci: Advanced Materials and Devices 2020;5:1–9.
[41] Canales D, Saavedra M, Flores MT, Bejarano J, Ortiz JA, Orihuela P, et al. Effect of bioglass nanoparticles on the properties and bioactivity of poly(lactic acid) films. J Biomed Mater Res 2020;108:2032–43.
[4][2] Serra T, Planell JA, Navarro M. High-resolution PLA-based composite scaffolds via 3-D printing technology. Acta Biomater 2013;9:5521–30.
[43] Baptista R, Guedes M, Pereira MFC, Maurício A, Carrelo H, Cidade T. On the effect of design and fabrication parameters on mechanical performance of 3D printed PLA scaffolds. Bioprinting 2020;20:e00096.
[44] Chen Z, Yan X, Yin S, Liu L, Liu X, Zhao G, et al. Influence of the pore size and porosity of selective laser melted Ti6Al4V ELI porous scaffold on cell proliferation, osteogenesis and bone ingrowth. Mater Sci Eng C 2020;106:110289.
[45] Huang Y, Chen F, Pan Y, Chen C, Jiang L, Dan Y. Effect of hydrophobic fluoropolymer and crystallinity on the hydrolytic degradation of poly(lactic acid). Eur Polym J 2017;97:308–18.
[46] Zhou X, Deng J, Fang C, Lei W, Song Y, Zhang Z, et al. Additive manufacturing of CNTs/PLA composites and the correlation between microstructure and functional properties. J Mater Sci Technol 2021;60:27–34.
[47] González P, Serra J, Liste S, Chiussi S, León B, Pérez-Amor M. Raman spectroscopic study of bioactive silica based glasses. J Non-Cryst Solids 2003;320:92–9.
[48] Balamurugan A, Sockalingum G, Michel J, Fauré J, Banchet V, Wortham L, et al. Synthesis and characterisation of sol gel derived bioactive glass for biomedical applications. Mater Lett 2006;60:3752–7.
[49] Vano-Herrera K, Vogt C. Degradation of poly(L-lactic acid) coating on permanent coronary metal stent investigated ex vivo by micro Raman spectroscopy. J Raman Spectrosc 2017;48:711–9.
[50] Cuiffo MA, Snyder J, Elliott AM, Romero N, Kannan S, Halada GP. Impact of the fused deposition (FDM) printing process on polylactic acid (PLA) chemistry and structure. Appl Sci 2017;7:579.
[51] Vidakis N, Petousis M, Velidakis E, Mountakis N, Tzounis L, Liebscher M, et al. Enhanced mechanical, thermal and antimicrobial properties of additively manufactured polylactic acid with optimized nano silica content. Nanomaterials 2021;11:1012.
[52] Ivanov E, Kotsilkova R, Xia H, Chen Y, Donato RK, Donato K, et al. PLA/Graphene/MWCNT composites with improved electrical and thermal properties suitable for FDM 3D printing applications. Appl Sci 2019;9:1209.
[53] Abeer M, El-Kady, Ali Ashraf F, Farag Mohmmad M. Development, characterization, and in vitro bioactivity studies of sol–gel bioactive glass/poly(l-lactide) nanocomposite scaffolds. Mater Sci Eng C 2010;30:120–31.
[54] Corcione CE, Gervaso F, Scalera F, Padmanabhan SK, Madaghiele M, Montagna F, Sannino A, Licciulli A, Maffezzoli A. Highly loaded hydroxyapatite microsphere/PLA porous scaffolds obtained by fused deposition modelling. Ceram Int 2019:2803–10.
[55] Baptista R, Pereira MFC, Maurício A, Rechena D, Infante V, Guedes M. Experimental and numerical characterization of 3D-printed scaffolds under monotonic compression with the aid of micro-CT volume reconstruction. Bio-Design and Manufacturing 2021;4:222–42.
[56] Baptista R, Guedes M. Morphological and mechanical characterization of 3D printed PLA scaffolds with controlled porosity for trabecular bone tissue replacement. Mater Sci Eng C 2021;118:111528.
[57] Bose S, Roy M, Bandyopadhyay A. Recent advances in bone tissue engineering scaffolds. Trends Biotechnol 2012;30(Issue 10):546–54.
[58] Schätzlein E, Kicker C, Söhling N, Ritz U, Neijhoft J, Henrich D, et al. 3D-Printed PLA-bioglass scaffolds with controllable calcium release and MSC adhesion for bone tissue engineering. Polymers 2022;14:2389.
[59] Lerman MJ, Lembong J, Muramoto S, Gillen G, Fisher JP. The evolution of polystyrene as a cell culture material. Tissue Eng B Rev 2018;24:359–72.
[60] Rosado-Galindo H, Domenech M. Polystyrene topography sticker array for cell-based assays. Recent Progress in Materials 2020;2:13.

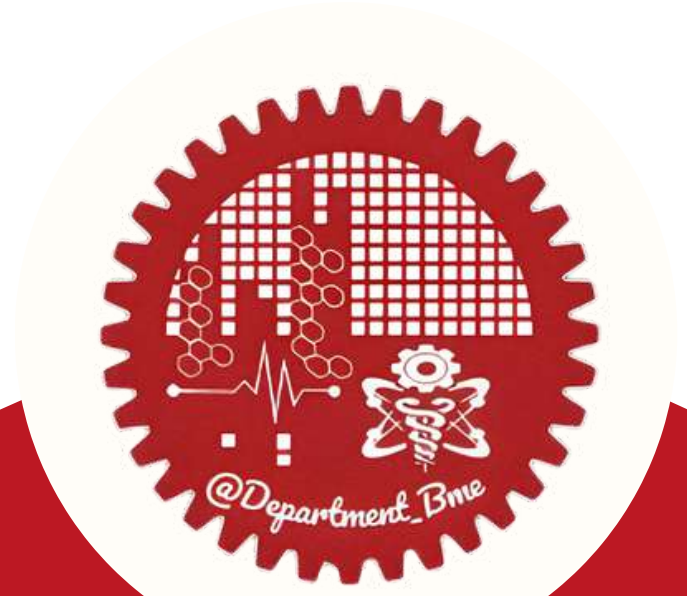

Contact Us

FOR MORE INFO

Department_bme

Info@dep-bme.ir

department_bme

Www.dep-bme.com